A simple model for nanofiber formation by rotary jet-spinning

Paula Mellado,[1,2] Holly A. McIlwee,[1,3] Mohammad R. Badrossamay,[1,3] Josue A. Goss,[1,3] L. Mahadevan,[1,2,4,a)] and Kevin Kit Parker[1,3,a)]
[1]*School of Engineering and Applied Sciences, Wyss Institute of Biologically Inspired Engineering, Harvard University, Cambridge, Massachusetts 02138, USA*
[2]*Kavli Institute for NanoBio Science and Technology, Harvard University, Cambridge, Massachusetts 02138, USA*
[3]*Disease Biophysics Group, Harvard Stem Cell Institute, Harvard University, Cambridge, Massachusetts 02138, USA*
[4]*Department of Physics, Harvard University, Cambridge, Massachusetts 02138, USA*

(Received 3 September 2011; accepted 20 October 2011; published online 15 November 2011)

Nanofibers are microstructured materials that span a broad range of applications from tissue engineering scaffolds to polymer transistors. An efficient method of nanofiber production is rotary jet-spinning (RJS), consisting of a perforated reservoir rotating at high speeds along its axis of symmetry, which propels a liquid, polymeric jet out of the reservoir orifice that stretches, dries, and eventually solidifies to form nanoscale fibers. We report a minimal scaling framework complemented by a semi-analytic and numerical approach to characterize the regimes of nanofiber production, leading to a theoretical model for the fiber radius consistent with experimental observations. In addition to providing a mechanism for the formation of nanofibers, our study yields a phase diagram for the design of continuous nanofibers as a function of process parameters with implications for the morphological quality of fibers. © *2011 American Institute of Physics*. [doi:10.1063/1.3662015]

The combination of high surface area (10^3 m^2/g),[1] mechanical flexibility, and directional strength make nanofibers an ideal platform for a diverse range of applications.[1–3] While nanofibers are most commonly produced using electrospinning,[4,5] we have recently demonstrated that rotary jet-spinning (RJS) can be used as an alternative technique to fabricate sub-micron fibers using rotational inertial forces to extrude viscous polymer jets.[6–8] Our apparatus consists of a perforated reservoir containing polymer solutions attached to a motor (Fig. 1(a)). When the reservoir is spun about its axis of symmetry at a rate larger than a threshold determined by the balance between capillary and centrifugal forces, a viscous jet is ejected from a small orifice (Fig. 1(b)). This jet is thrown outwards along a spiral trajectory as solvent evaporates, owing to its relatively high surface area (Figs. 1(c)–1(f)). While moving, it is extended by centrifugal forces (Figs. 1(g)–1(j)) and solvent evaporates at a rate J, dependent on the diffusion coefficient D of solvent through the polymer (Fig. 1(k)). The jet travels until it reaches the walls of the stationary cylindrical collector of radius R_c. Once there, the remaining solvent evaporates, fibers solidify, and may be collected.

To quantify the dynamics of jet spinning and understand the relative role of surface tension, inertial, non-inertial, and viscous forces, we use scaling ideas to distinguish between three main stages of the process: (1) jet initiation, (2) jet extension, and (3) solvent evaporation. These three stages are characterized by the ejection time scale $\tau_1 \sim 1/\Omega_{th}$ proportional to the inverse of the critical angular speed Ω_{th} for which the jet is able to come out of the orifice (Fig. 1(c)), the viscous time scale $\tau_2 \sim r^2\rho/\mu$ of the polymer with extensional viscosity μ and density ρ (Fig. 1(g)), and the solvent evaporation time scale $\tau_3 \sim r^2/D$ controlling the internal diffusion of solvent through the drying polymer (Fig. 1(k)). The ratio $\tau_2/\tau_3 \sim 10^{-2}$ marks a clear separation between the extension and solvent evaporation stages.

High speed imaging shows average time for a fiber to reach a collector of radius $R_c = 13.5$ cm, when the reservoir is rotated at an angular speed $\Omega \sim 12\,000$ rpm, $t_{gap} \sim 4 \times 10^{-2}$ s, which is consistent with the simple scaling $t_{gap} \sim 1/\Omega \sim 10^{-2}$ s. Measurements of solvent evaporation rate J provide evidence that under ambient conditions, the solvent evaporates after a time $t \gg t_{gap}$. This is because solvent evaporation is dominated by internal solvent diffusion through the polymer to the surface of the liquid jet[9] over a time scale $\tau_3 \sim r^2/D$, where $D \sim 10^{-7}$ cm^2/s is the diffusion coefficient of the solvent in the polymer[10] and r is jet radius. From dimensional arguments, it is evident that at a solvent concentration of 90 wt. %, for instance, the ratio between the initial and final volume of the jet, when solvent has evaporated is $v_f = 0.1 v_{in} \sim 10$. Thus, in this approximation, the radius r decreases to 1/3 the initial value if all the solvent evaporates. Fig. S2 (Ref. 14) shows that for r to decrease to 1/3, its initial radius $r_0 \sim a/3$, the time elapsed is $t_{r0/3} \sim 250$ s. Setting $\tau_3 = t_{r0/3}$, yields $\tau_r \sim a/3$ and consequently $t_{gap}/\tau_3 \sim 10^{-4}$. The timescale of solvent evaporation was measured as solvent evaporated from the fiber mass after spinning. Evaporation was visualized by incorporation of a solvent sensitive dye into polymer solutions prior to spinning (Fig. 1(l)).[11,14] Both theory and experiment show that most solvent evaporates after fibers have landed on the collector walls. Therefore, jet extension dominates the process controlling fiber radius.

The first stage of fiber formation is jet initiation. Since the hydrostatic pressure $\rho g h$ at the orifice is three orders of

a)Authors to whom correspondence should be addressed. Electronic addresses: kkparker@seas.harvard.edu and lm@seas.harvard.edu.

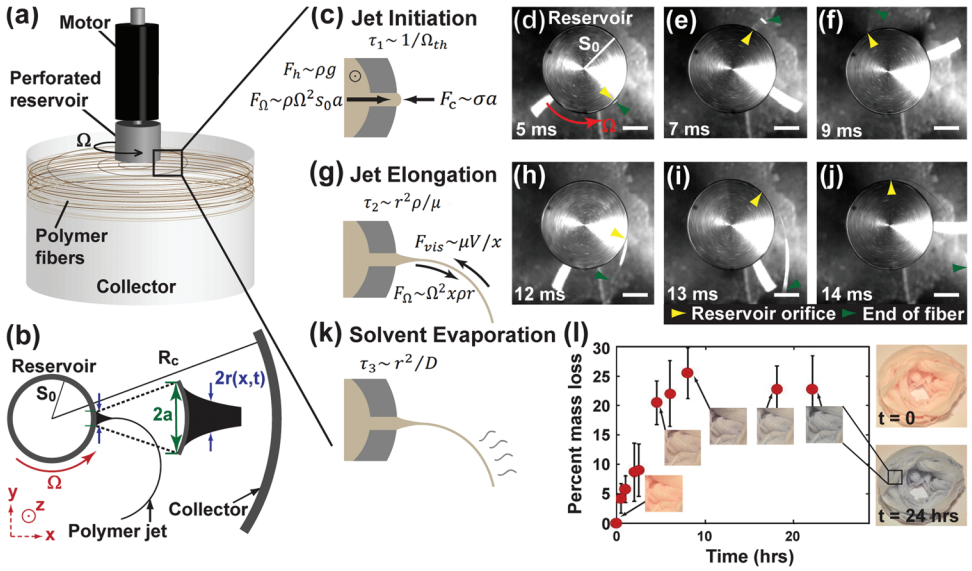

FIG. 1. (Color) (a) Schematic of RJS apparatus. (b) Top view diagram of a fiber projecting from the reservoir, towards the collector. (c)-(f) Jet initiation. (d)-(f) Photographic images capture initiation of the jet from the reservoir. Green arrows denote the end of the jet and yellow arrows mark orifice position. (g)-(j) Jet elongation. In (d)-(f) and (h)-(j), $s_0 = 0.85$ cm and scale bars are 0.42 cm. (k) Solvent evaporation. (l) Fiber color is an indication of the presence of solvent in the collected fibers, as solvent evaporates, fiber color changes from red to blue. Color evolution is in good agreement with the measured mass change of the collected fibers.

magnitude smaller than the centrifugal force $\rho\Omega^2 s_0 a$ at the orifice of radius a in the reservoir of radius s_0, its role in jet ejection is negligible. Then, balancing inertial force $\rho\Omega^2 s_0 a^3$ with the capillary force at the orifice on the reservoir, σa, yields a critical rotational speed for jet ejection $\Omega_{th} \sim \sqrt{\sigma/a^2 s_0 \rho}$ and an ejection speed $V \sim \Omega_{th} s_0$. Once the polymer jet exits the orifice, its extension is driven by the balance between viscous and centrifugal forces in the second stage of fiber formation. Noting that the viscous elongational stress on a jet of radius r and velocity V being stretched axially scales as $\mu V/x$, where x is the distance from the orifice, and mass conservation implies that $Ua^2 = Vr^2$, we get an expression for the jet radius as a function of the experimental parameters that reads

$$r \sim \frac{aU^{1/2}\nu^{1/2}}{R_c^{3/2}\Omega}, \tag{1}$$

where a is the initial jet radius, $\nu = \mu/\rho$ is the kinematic viscosity, and $x \sim R_c$ is the collector radius ($R_c \gg s_0$).

To test Eq. (1), poly(lactic acid) (PLA) fibers were fabricated using different experimental conditions.[14] The radius of the collector R_c, viscosity μ, angular speed Ω, and orifice radius a were changed to span a range of fiber radii of one decade. PLA concentration varied from 4 to 9.5 wt. % in chloroform, Ω from 4000 to 37 000 rpm, and R_c from 9 to 18 cm. Polymer concentration changed the viscosity of prepared samples from 25 to 250 mPa·s.[14] Surface tension and density of the samples remained approximately constant as polymer concentration was changed.[14] Fig. 2(a) shows fiber radius versus Eq. (1). This scaling law can be used to predict fiber radius and is shown to hold for multiple experimental schemes (Fig. 2(a)). The data are best fitted by the power law $\left(\frac{a^2 U\nu}{\Omega^2 R_c^3}\right)^{1/2} \sim r^{1.09\pm0.05}$ marked by the dashed line in Fig. 2(a), in good agreement with Eq. (1).

To obtain additional information regarding how the size of the jet scales with μ and Ω, the dynamics of extension were examined in further detail by studying a simplified one-dimensional (1-D) theory for the fluid jet, assumed to be incompressible, Newtonian and isothermal. Making use of its slenderness,[12] we use a 1-D model set of equations in the axial coordinate x for the conservation of mass and momentum[13,14] including effects of capillarity, inertial, viscous, and external body forces. Solving the resulting 1-D transient model numerically and approximate 1-D steady state model analytically, we see there is good agreement (Fig. S1 (Ref. 14)) between experimental results, the simple steady state scaling law (Eq. S4 (Ref. 14)) and the transient solution.

The range of variability of μ and Ω, which permit fiber formation, is summarized in the phase diagram in Fig. 2(b). Across the range of μ and Ω investigated, three regimes exist experimentally. In regime I, where Ω, μ, or both are large enough, continuous fibers, defined as those samples with less with 5% beads or defects, are produced. For example, at high angular speeds, $\Omega \sim 30\,000$ rpm, continuous fibers are formed using concentrations between 4 wt. % and 9 wt. % spanning one decade in solution viscosity (regime I) (Fig. S2(a) (Ref. 14)). Scanning electron microscopy (SEM) images show fiber morphology of samples within regime I: fine continuous nanofibers collected from medium viscosity solutions (Figs. 2(d) and 2(g)) and large continuous microfibers collected from high viscosity solutions (Figs. 2(e) and 2(h)). Open data points in Fig. 2(b) mark the lower limit of Ω for which continuous fibers prepared from solutions across the range of concentrations were collected.

As we decreased the viscosity of the solution, it was necessary to increase the angular velocity in order to produce collectable, continuous fibers. This was the case at 5.8 wt. % and $\Omega = 8000$ rpm, where continuous fibers were produced (regime I). As Ω, μ, or both decrease to moderate values, regime II emerges where fibers can be fabricated, but beads or other defects are also produced. When the same 5.8 wt. % solution was spun at $\Omega = 6000$ rpm, beaded fibers resulted (regime II). Beads or defects form because the centrifugal force is not large enough to overcome surface tension and elongate the jet before it reaches the collector. SEM images show beaded fibers collected in regime II from low viscosity solutions spun at high speeds (Figs. 2(c) and 2(f)). Filled data points in Fig. 2(b) mark the transition from regime II where beaded fibers are fabricated to regime III where Ω, μ, or both are too small to fabricate fibers. For all solutions in the range

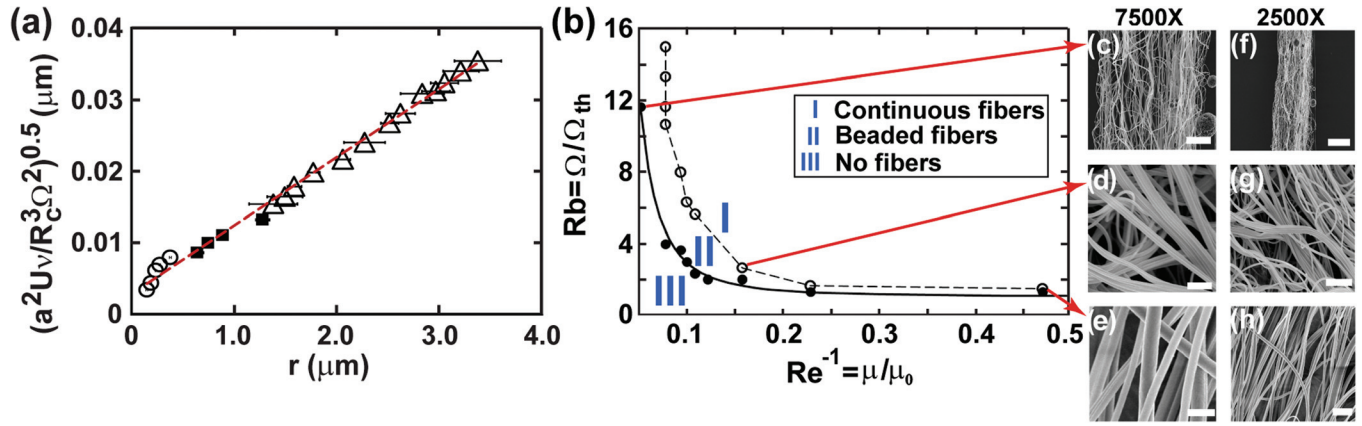

FIG. 2. (Color) (a) Fiber radius measurements. Circles: $a = 230\,\mu$m. Squares: $R_c = 13.5$ cm, $\mu = 113$ mPa·s, and $a = 230\,\mu$m. Triangles: $R_c = 13.5$ cm, $\mu = 113$ mPa·s, and $a = 410\,\mu$m. Data are best fitted by $(a^2Uv/R_c^3\Omega^2)^{0.5} \sim r^{1.09\pm0.05}$ (red dashed line). (b) A phase diagram divides the scaled angular velocity—viscosity (the Rossby number, $Rb = \Omega/\Omega_{th}$, Ω_{th} being the threshold speed for fibers to exit the reservoir, and the Reynolds number, $Re = \mu/\mu_0$, where $\mu = \sqrt{\sigma s_0 \rho}$) plane into regimes I, II, and III. Open circles: transition to collecting beady fibers (regime II). Solid circles: transition to values at which no fibers can be collected (regime III). The boundary between regime II and III best fits the function $\Omega_c \sim \mu^{-2.88\pm0.25}$ (black curve). (c)-(h) SEM images showing fiber morphology of samples from different regimes at 2500X and 7500X magnifications. (c) and (f) Beady fibers are collected in II ($\mu = 0.025$ Pa·s, $\Omega = 35\,000$ rpm, and 8% beads). (d) and (g) Fine continuous fibers collected in I ($\mu = 0.079$ Pa·s and $\Omega = 8000$ rpm). (e) and (h) Large continuous fibers collected in I ($\mu = 0.178$ Pa·s and $\Omega = 4800$ rpm). Scale bar is 4 μm (c)–(e) and 20 μm (f)–(h).

of polymer concentrations described above spun at $\Omega = 2000\,\text{rpm} < \Omega_{th}$, $a = 230\,\mu$m, and $R_c = 13.5$ cm, no fibers formed (regime III). At $\Omega = 3000\,\text{rpm} \sim \Omega_{th}$, fiber jets could be visualized leaving the reservoir though no solid fibers could be collected. In this case, the centrifugal force was not enough to facilitate the jet reaching the collector (regime III). The range of Ω and μ explored in the phase diagram represents the parameter space necessary to produce both continuous and beaded fibers from solutions of PLA in chloroform based on rheological behavior.

The scaling law (Eq. (1)) describes how fiber radius shrinks as we move toward larger Ω and μ, inside regimes I and II. The transition between regime II and III can be explained with dimensional arguments in terms of the time for capillary induced breakup of a stationary jet $t_c \sim \frac{\mu r}{\sigma}$.[9] Comparing this time scale with that for the advective motion of the jet from the reservoir to the collector, $t_{gap} \sim 1/\Omega$ and using Eq. (1) for the jet radius, we find that the minimum angular speed for fiber formation is $\Omega_c \sim \frac{\rho R_c^2 \sigma^2}{a^2}\mu^{-3}$. This power law determines the transition between the regimes where no fibers can be created (III) and where fibers with beads or malformations are produced (II), consistent with experimental observations as shown in Fig. 2(b). As expected, the boundary between regimes II and III is best fit by the power law $\Omega \sim \mu^{-2.88\pm0.25}$ as shown by the continuous curve in Fig. 2(b).

Our combined experimental and theoretical study of the formation of polymeric fibers produced by RJS shows that fiber radius follows a simple scaling law (1) that characterizes how RJS-manufactured nanofiber radius is tuned by varying viscosity, angular speed, distance to the collector, and the radius of the orifice by studying forces governing the stages of fiber formation. A phase diagram for the design space of continuous nanofibers as a function of process parameters is in good agreement with experiments and has implications for the production rates as well as in the morphological quality of fibers with radius ranging from 150 nm–3 μm.

We acknowledge financial support of this work from Wyss Institute for Biologically Inspired Engineering, Harvard University Materials Research Science and Engineering Center (MRSEC), Harvard University Nanoscale Science and Engineering Center (NSEC), Defense Advanced Research Projects Agency (DARPA W911NF-10-1-0113), Harvard Center for Nanoscale Systems (CNS). H.A.M acknowledges the National Science Foundation Graduate Research Fellowship Program. P.M. and H.A.M. contributed equally to this work.

[1]E. P. S. Tan and C. T. Lim, Compos. Sci. Technol. **66**, 1102 (2006).
[2]D. R. Nisbet, J. S. Forsythe, W. Shen, D. I. Finkelstein, and M. K. Horne, J. Biomater. Appl. **24**, 7 (2009).
[3]G. G. Tibbetts, M. L. Lake, K. L. Strong, and B. P. Rice, Compos. Sci. Technol. **67**, 1709 (2007).
[4]S. V. Fridrikh, J. H. Yu, M. P. Brenner, and G. C. Rutledge, Phys. Rev. Lett. **90**, 144502 (2003).
[5]S. A. Theron, E. Zussman, and A. L. Yarin, Polymer **45**, 2017 (2004).
[6]M. R. Badrossamay, H. A. McIlwee, J. A. Goss, and K. K. Parker, Nano Lett. **10**, 2257 (2010).
[7]T. Senthilram, L. A. Mary, J. R. Venugopal, L. Nagarajan, S. Ramakrishna, and V. R. G. Dev, Mater. Today **14**, 226 (2011).
[8]M. Huttunen and M. Kellomaki, J. Tissue Eng. Regener. Med. **5**, e239 (2011).
[9]N. Kojic, M. Kojic, S. Gudlavalleti, and G. McKinley, Biomacromolecules **5**, 1698 (2004).
[10]F. R. Perioto, M. E. T. Alvarez, W. A. Araujo, M. R. Wolf-Maciel, and R. M. Filho, J. Appl. Polym. Sci. **110**, 3544 (2008).
[11]J. Yoon, Y -S. Jung, and J. M. Kim, Adv. Funct. Mater. **19**, 209 (2009).
[12]S. Panda, N. Marheineke, and R. Wegener, Math. Methods. Appl. Sci. **31**, 1153 (2008).
[13]N. Marheineke and R. Wegener, J. Fluid Mech. **622**, 345 (2009).
[14]See supplementary material at http://dx.doi.org/10.1063/1.3662015 for experimental and numerical methods.